*Journal of Zhejiang University-SCIENCE A (Applied Physics & Engineering) in press*
www.jzus.zju.edu.cn; www.springer.com/journal/11582
E-mail: jzus_a@zju.edu.cn

**Research Article**

https://doi.org/10.1631/jzus.A2400513

# Design and fabrication of biomimetic four-region drug-laden cartilage scaffolds with porous hollow fibers

Yu CHEN[1,2], Yuzhe MA[1,2], Jianzhong FU[1,2], Xinhua YAO[1,2]✉

[1]*State Key Laboratory of Fluid Power and Mechatronic Systems, School of Mechanical Engineering, Zhejiang University, Hangzhou 310058, China*
[2]*Key Laboratory of 3D Printing Process and Equipment of Zhejiang Province, School of Mechanical Engineering, Zhejiang University, Hangzhou 310058, China*

**Abstract:** Articular cartilage, which plays a vital role in joint structure, is susceptible to damage from trauma and degenerative joint diseases. Traditional methods for cartilage treatment often involve complex surgical procedures with limited efficacy. Alternatively, implantable drug-loaded scaffolds are an increasingly attractive cartilage treatment option. To address the challenges of structural and functional compatibility between scaffolds and native cartilage, as well as issues related to drug loading, we design a novel cartilage scaffold with a four-region hollow porous fiber network structure. Using an extrusion-based 3D printing platform, a biphasic silicone ink composed primarily of liquid-phase silicone and solid particles was employed to construct the hollow porous fiber network. Mechanical compression tests demonstrate that the cartilage scaffold has mechanical characteristics similar to those of native cartilage tissue, and ultraviolet spectrophotometry measurements confirm its ability to control drug release. These results showcase the feasibility and effectiveness of the proposed cartilage substitute structure.

**Key words:** Bionic design; 3D printing; Cartilage scaffold; Gradient porous structure; Regulation of mechanical properties; Drug delivery systems

Unedited

## 1 Introduction

Articular cartilage defects represent a serious medical issue, as they frequently result in severe disability for patients. Due to the extremely limited regenerative capacity of articular cartilage (Liu et al., 2018), its damage or degeneration can lead to chronic pain and functional impairment. Thus, developing effective clinical methods to treat cartilage injury is of paramount importance (J.X. Liu, 2019; Schizas et al., 2019). Among novel methods, implanting scaffolds at the injury site to mimic cartilage function has emerged as a promising treatment (Zhang et al., 2019; Hua et al., 2022; Shen et al., 2024; Yang et al., 2024a; Yang et al., 2024b). However, current scaffold implantation therapies face numerous challenges in clinical application, such as the need for complex surgical procedures (Kwon et al., 2019), significant immune rejection (Soleymani et al., 2024), mechanical property mismatch with native cartilage (Zhang et al., 2022), inadequate viscoelasticity, the limited unifunctional nature of certain scaffolds, and other factors. So despite recent advancements, scaffold implantation treatment leaves much to be desired. Its associated issues often result in treatment delays and subpar clinical outcomes compared to expectations.

Optimized cartilage scaffold design is imperative when replacing native cartilage to treat degenerative diseases (Liu et al., 2019; Malda et al., 2019). As understanding of native cartilage structure has advanced, cartilage scaffold design has progressed from simple monophasic models to more sophisticated biphasic, triphasic, and multiphasic constructs. These advancements aim to improve upon early designs, which failed to represent the complex structure of native cartilage. For instance, monophasic collagen scaffolds with radially aligned and randomly arranged collagen fibers were recently

✉ Xinhua YAO, yaoxinhuame@zju.edu.cn

Received Nov. 10, 2024; Revision accepted Mar. 24, 2025; Crosschecked

© Zhejiang University Press 2025

designed and fabricated (Chen et al., 2015). While these scaffolds have shown promise in promoting mesenchymal stem cell migration and healing in vitro, they do not replicate the full depth and functional complexity of native cartilage. Studies on mesenchymal stem cell migration (in vitro) and bone-cartilage defect repair (in vivo) have demonstrated that radially aligned collagen fiber scaffolds perform well in promoting cell migration and healing. Following 26 weeks of implantation in goats, comparative analyses between collagen/glucosamine biphasic scaffolds and polylactic/polyglycolic acid biphasic scaffolds in terms of morphology, histology, and mechanical properties revealed that the collagen/glucosamine biphasic scaffold was more effective in treatment of degenerative cartilage disease (Getgood et al., 2012). However, while biphasic scaffolds help regenerate cartilage and bone layers, they fail to address the calcified cartilage layer, which is a critical component for interface integration; this can lead to delamination between layers and failures in tissue repair. In another study using iterative freeze-drying technology, triphasic scaffolds based on hyaluronic acid, Type I collagen, and hydroxyapatite were prepared, with Type II collagen added in the middle and upper layers to mimic natural cartilage components (Levingstone et al., 2016a; Levingstone et al., 2016b). These scaffolds enabled long-term repair of goat articular cartilage, effectively simulating the hierarchical structure of the cartilage-bone interface. Nevertheless, this scaffold type still failed to achieve tight integration with the surrounding tissue.

Currently, gradient scaffolds are attracting increasing attention, as they more accurately mimic primary cartilage tissue and possess gradient chemical compositions and structural characteristics (Parisi et al., 2020; Wang et al., 2024b). For example, selective laser sintering technology was used to prepare a seven-layer gradient scaffold with poly(ε-caprolactone) and hydroxyapatite microspheres as the substrate (Du et al., 2017). Additionally, the combination of poly( ε -caprolactone) (PCL) and hydrogel components such as methacrylated hyaluronic acid (MeHA) in scaffolds has been used to enhance angiogenesis and tissue regeneration in cell transplantation therapy (Yang, et al., 2024a). Moreover, silk fibroin-DNA hydrogel-based microspheres (RSD-MSs) were developed to enhance cartilage repair, as they possess the potential to promote chondrogenic differentiation of bone marrow stem cells (BMSCs) and facilitate cartilage regeneration (Shen, et al., 2024). Both in vitro and in vivo experiments have confirmed the role of scaffolds with complex structures or composite materials in promoting osteochondral repair and regeneration. However, such scaffolds still lack full biological functionality, with natural tissue integration and sustained biological activity remaining major limitations.

In recent years, cartilage scaffolds with varying chemical compositions and structural characteristics have been explored. However, monophasic scaffolds still fail to replicate the stratified structure of osteochondral units, which is essential for effective damage treatment and natural cartilage replacement. Although biphasic scaffolds have shown promise in promoting regeneration of cartilage and bone layers, they often neglect the calcified cartilage layer, which results in poor integration between scaffold and cartilage. This can lead to delamination between layers and, ultimately, failed cartilage treatment (Da et al., 2013). Furthermore, the limited metabolic capacity of cartilage tissue hinders development of strong bonds between the scaffold and natural tissue. Therefore, a major goal is to design scaffolds with inherent tissue integration capabilities, so as to ensure long-term functionality, stable biological fixation, and appropriate mechanical conduction following implantation (Pattnaik et al., 2023). Incorporating drug delivery systems into scaffolds promotes improved integration between the scaffold and the implant site, minimizes inflammation during healing, and extends the retention time of therapeutic agents, ensuring their sustained action at the damaged site (Kim et al., 2021; Han et al., 2023). However, research on biomimetic cartilage scaffolds that can simultaneously replicate the structure and biological functions of native cartilage remains in its infancy. To improve treatment of cartilage damage, it is crucial to develop scaffolds that both match the mechanical properties of native cartilage and integrate effective drug delivery systems.

To improve mechanical performance matching and drug-coordinated biological function in cartilage scaffolds (Wang et al., 2024a; Yang, et al., 2024b),

Unedited

we propose a novel biomimetic four-region drug-loading porous cartilage scaffold structure. Addressing mechanical mismatch, a four-region biomimetic 3D fiber network structure with adjustable structural parameters was designed, inspired by the native four-region architecture of cartilage. The fiber structure within each region of the cartilage scaffold differs in diameter, spacing, and arrangement. Utilizing extrusion-based 3D printing technology with controlled printing paths and process parameters, we achieved zonal construction and integration of the cartilage scaffold with effective matching to the mechanical properties of native cartilage. In the context of drug-coordinated treatment, the scaffold fibers were designed to be internally hollow and porous-walled. As water penetrates the scaffold, it dissolves the drug powder within the fiber walls and the resulting solution is stored in the fiber tube pores. When the scaffold is compressed, drugs are slowly released under capillary action, thus achieving functionalities of loading and sustained release. The proposed biomimetic drug-loading cartilage scaffold offers a novel therapeutic approach for degenerative cartilage diseases.

## 2 Materials and methods

### 2.1 Materials

A shear-thinning PDMS material SE 1700 and a low-viscosity PDMS material Sylgard 184 were sourced from Dow Corning (Auburn, MI, USA). Sodium hydrogen carbonate (NaHCO3), sodium chloride (NaCl), hydrochloric acid (HCl), ethanal, and toluene were acquired from Sinopharm (Beijing, China). Deionized water, cetyltrimethyl ammonium bromide (CTAB), tetraethyl orthosilicate (TEOS), (3-Aminopropyl) triethoxysilane (APTES), gallium (III) nitrate hydrate (Ga(NO3)3·nH2O), rhodamine B, titanium chloride solution (TiCl3), and 4-methyl-2-pentanone were sourced from Aladdin (Shanghai, China). All other chemicals and reagents used were of analytical grade and did not require further purification. Liquid nitrogen was sourced from Otterson (Zhejiang, China). Phosphate-buffer saline (PBS) and trypsin were acquired from Gibco (California, USA). Human chondrosarcoma cell lines SW 1353 and L-15 medium were obtained from Zhong Qiao Xin Zhou (Shanghai, China).

### 2.2 Materials

Biphasic viscoelastic PDMS inks are prepared by blending two silicone elastomers in liquid phase: SE 1700 and Sylgard 184 (which is used to dilute SE 1700 for appropriate rheological properties), and particles in solid phase: NaCl and NaHCO3 (which are used as pore-forming agents). Both SE 1700 and Sylgard 184 base materials are mixed with their curing agents in a 10:1 (base: curing agent) ratio by weight prior to blending. NaCl particles are ground with a planetary ball mill JX-2G (Jingxin, Shanghai, China) and sieved in 150 mesh before blending. The final inks are loaded into a 5-cc syringe barrel at room temperature and spun in a high-speed centrifuge TG16-WS (Cence, Hunan, China) at 5000 r/min for 5 min to remove air bubbles.

### 2.3 Preparation for 3D printing

3D printing is performed using a BP6601 3D bioprinter (EFL, Suzhou, China) with an in-situ curing device. The biphasic viscoelastic PDMS inks are loaded into 5-cc syringe barrels at room temperature, which are then capped with co-axial nozzles. The co-axial nozzles are equipped with an 18GA (d850 μm) outer nozzle and a 28GA (170μm) inter nozzle which is blocked with a solid pin. A unit with a built-in air pump is used to control the extrusion pressure. The printing speed is managed with a program (G-code) that is sent to the printer using Repetier software. The parameters of the 3D printing process are shown in Table 1.

**Table 1 Extrusion 3D printing process parameters**

| Extrusion pressure | In-situ curing temperature | Printing speed | First-laye r height | Interlayer height |
|---|---|---|---|---|
| 160 kPa | 160℃ | 1.8 mm/s | 1.3 mm | 1.2 mm |

### 2.4 Preparation of the biomimetic four-region drug-laden porous cartilage scaffold

Overall, the scaffold has a hollow fiber network structure, which can be divided into four regions from bottom to top: a shallow region structure with relatively small fiber diameter and cross-arranged fibers; a transition region structure with many diagonal fibers with relatively large fiber diameter; a radial region structure with the largest diameter cross-arranged fibers; and a calcified cartilage region

Unedited

with dense fibers. Each four-region drug-loaded porous cartilage scaffold was fabricated through 3D printing and in-situ curing using biphasic silicone ink. Then, pore-forming agents such as sodium chloride and sodium bicarbonate were removed through placement in a water bath. The final scaffolds were obtained after drying in a 40℃ chamber for 20 minutes.

### 2.5 Simulation of the cartilage scaffold structure

We developed numerical models for the compressional mechanical properties of the cartilage scaffolds, so as to determine optimal structural design parameters including fiber diameter, fiber distance, and fiber arrangement angle. The simulations were 3D finite-element models in COMSOL Multiphysics 6.0. Mooney-Rivlin constitutive model parameters for hyperelastic materials were fit to uniaxial tensile data from the type II dumbbell PDMS standard specimen. Fixed constraints were applied to the bottom surface of the geometric model in the negative z-direction, with displacement along this direction being specified at the opposite end of the model. No additional settings were required for the other surfaces. The constitutive parameters of the Mooney-Rivlin models were $C_{10}$ = 46,617 Pa, $C_{01}$ = $3.0974\times10^{5}$ Pa, and $D_1$ = $1.2861\times10^{-6}$ Pa. Scaffold samples with different structural design parameters were then modeled through orthogonal experiment design.

### 2.6 Surface topography and porosity

A cartilage scaffold sample was printed for morphological observations and porosity evaluation, with an overall size of 8 mm × 8 mm × 15 mm. The printed sample was placed in a water bath and heated until boiling, such that solid particles and holes were removed by the water. A front image of the cartilage scaffold sample was captured by a macro camera, and then the cross section of the empty fiber structure was imaged using a scanning electron microscope (SEM; Zeiss, Germany). The threshold segmentation function in the ImageJ software was used to screen the pore region, measure the total number of pixels in the pore region, and calculate its porosity ( $\varphi_P$ ) according to the following formula:

$$\varphi_P = \frac{A_P}{A_{all}} \times 100\% \tag{1}$$

### 2.7 Mechanical properties

A uniaxial compression test is performed to obtain the stress-strain curve, and thus verify the validity of the simulation model in characterizing the mechanical properties of the scaffolds. The mechanical properties of the designed cartilage scaffold are mainly related to three structural parameters: fiber diameter, fiber spacing, and fiber arrangement direction. In order to explore the influence of various parameters on the mechanical properties of cartilage scaffolds, 25 groups of simulation analysis models were constructed according to the mixed horizontal orthogonal tests of one factor, three levels, two factors, five levels, and the pseudo-horizontal method (Fig. 1). The initial length and width of each sample were first measured, and the cross-sectional area of the scaffold was calculated. Then a preload was slowly applied to the sample. The compression rate was set to 10 mm/min. After the scaffold was compressed to 20% of its original length, the compression modulus was estimated using the slope of the initial linear region of the stress-strain curve.

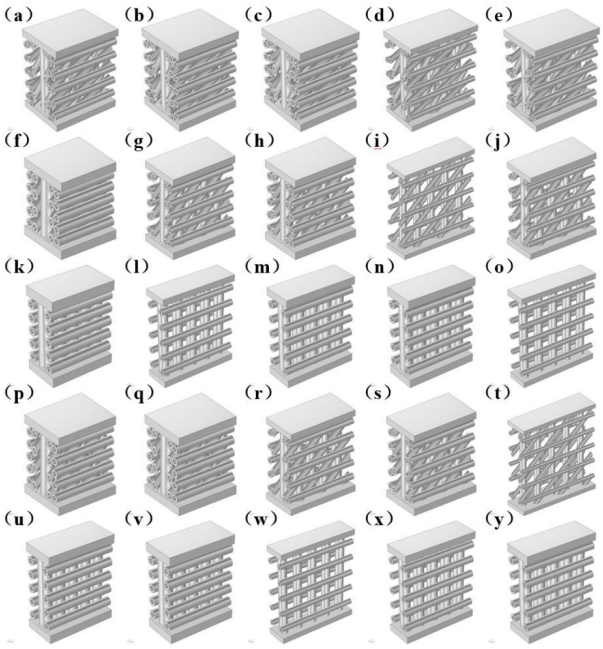


**Fig. 1 COMSOL Mutliphysics parametric geometric modeling**

Unedited

### 2.8 Sustained drug release properties

A gallium complexing compound was first produced through reaction of gallium nitrate solution with rhodamine B in acidic conditions. Then the standard curve of the gallium complexing compound was measured under the maximum absorption peak using a UV spectrophotometer (Shimadzu, Japan). The scaffolds were submerged in 20 mL of deionized water, then simultaneously, 5 mL of gallium (III) nitrate sustained-release solution was extracted and 5 mL of deionized water was replenished. These samples of solution were extracted at times of 1 h, 2 h, 4 h, 6 h, 8 h, 12 h, 24 h, 48 h, and 72 h in 0%, 5%, 10%, 15%, and 20% compression conditions. Subsequently, samples were reacted with rhodamine B in acidic conditions to obtain the gallium complexing compound. Then, the absorbance of each gallium complexing compound was measured by the UV spectrophotometer under the maximum absorption peak. Finally, the concentration of gallium (III) nitrate was determined based on the standard premeasured curve (Zhou B, 2005). The cumulative release percentage of gallium (III) nitrate ( $p_n$ )was calculated by:

$$p_n = \frac{c_n v_n + \sum_{i=1}^{n} c_i v_i o_i}{m} \times 100\% \quad (2)$$

where $c_n$ is the concentration of gallium (III) nitrate in sample $n$ , $v_n$ is the residual volume of deionized water in sample $n$ , $c_i$ is the concentration of gallium (III) nitrate in sample $i$ , $v_i$ is the extracted volume in sample $i$ , $o_i$ is the dilution ratio of the solution in sample $i$ , and m is the mass of gallium (III) nitrate.

### 2.9 Cytocompatibility evaluation

2.9.1. Cell culture

SW1353 was cultured in an L15 medium (Leibovitz) supplemented with 10% fetal bovine serum (Gibco,USA) and a 1% penicillin-streptomycin formulation (Gibco, USA) at 37°C with 5% CO2.

2.9.2. Cytocompatibility test

SW1353 was cultured on the scaffold for 48 hours before the biocompatibility test. The cytotoxicity of the scaffolds under different treatments was then measured using a Calcein-AM(Calcein acetoxymethyl ester)/PI (Propidium Iodide) Viability/Cytotoxicity Kit (Solarbio, Beijing) according to the manufacturer's protocol.

2.9.3. Statistical analysis

Statistical analysis was performed using OriginPro 9.1 and GraphPad Prism 8.0. All experiments involved at least triplicate samples, and the data was presented with the mean ± standard deviation (SD). Two-sided $p < 0.05$ was used as the criterion for statistical significance.

## 3 Results and discussion

### 3.1 Bionic design method and manufacturing process of the cartilage scaffold

Articular cartilage is a special connective tissue that covers the ends of joints. Its smoothness and wear-resistance enable it to slide and absorb impact forces when a joint moves slightly, enabling the joint to withstand high cyclic loads (Gu et al., 2023).Articular cartilage consists mainly of sparse chondrocyte populations embedded in a broad extracellular matrix (Sun et al., 2020). The unique biological and biomechanical properties of articular cartilage are intrinsically linked to its structure and composition, as well as to the interactions between chondrocytes and the extracellular matrix. Morphologically, mature articular cartilage can be divided into four distinct regions from shallow to deep: the superficial layer consists of thin, dense collagen fibers, which are mainly used to resist tensile stress. The transitional layer is composed of diagonal collagen fibers of large diameter, and is mainly responsible for bearing compressive stress. The radiation layer is composed of the largest-diameter collagen fibers and also acts to resist compressive stress. Finally, the calcified cartilage layer is characterized by thick and densely arranged collagen fibers, whose function is to anchor the cartilage to the underlying bone.

To enable cartilage scaffolds to replicate the mechanical function of natural cartilage and facilitate synergistic treatment through slow drug release, the proposed scaffold structure is that of a three-dimensional network composed of hollow porous fibers stacked at a certain angle. The four-region structure of the cartilage scaffold mimics

Unedited

natural cartilage, and can be divided into four regions: the superficial region, transitional region, radial region, and calcified cartilage layer (Fig. 2a). The structural parameters of each region are closely related to their mechanical properties. Through path planning and parameter adjustment for the 3D printing, four regions of the scaffold were manufactured with different structural parameters (Fig. 2a). During the preparation of the cartilage scaffolds, gallium nitrate powder was embedded into the fibrous wall of the scaffold. After implantation, water in the body flows through the hollow fiber tube due to "capillary effects" (Li et al., 2021). The gallium nitrate particles embedded in the fiber wall dissolve in the gallium ion water solution and are stored in the pores of the tube wall. When the scaffold is compressed, the scaffold slowly releases gallium nitrate solution instead of discharging it all at once due to the "capillary effect" (Cai et al., 2022). Therefore, this structure enables the proposed cartilage scaffold to facilitate long-term drug release and match mechanical functions of natural cartilage, thereby improving treatment efficacy (Fig. 2a). A macroscopic image of the scaffold and an SEM image of a single hollow porous fiber (Fig. 2b) showcase the hollow structure. Notably, after the pore-forming agent was removed during the water bath, it was observed that the particles formed different pore sizes. The porosity ( $\varphi_P$ ) calculated from Eq. (1) was 60.19%, thus providing ample space for cell growth and drug release.

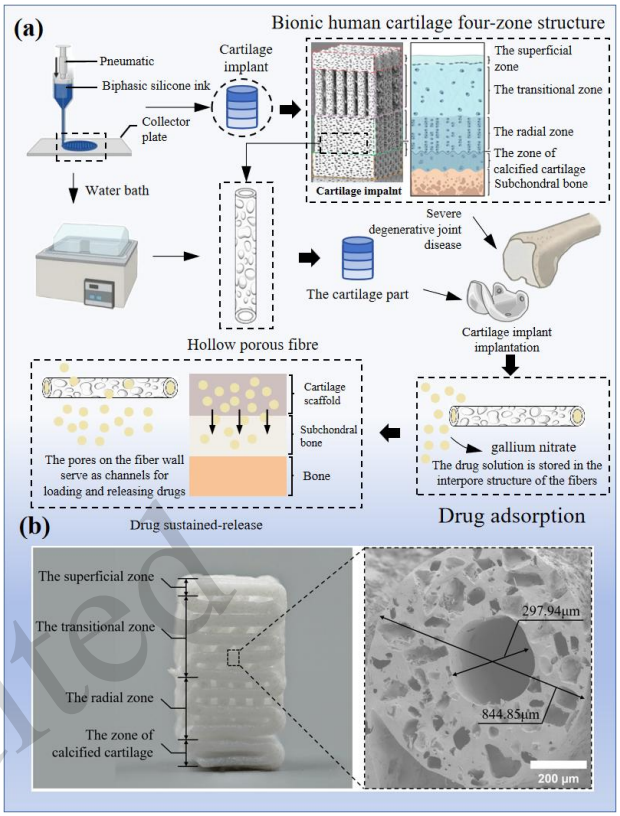


**Fig. 2 Bionic design and fabrication of cartilage scaffold structure**

(a)Bionic four-region drug-loaded porous cartilage scaffold; (b)Morphological characteristics of the bionic four-region drug-carrying porous cartilage scaffolds

## 3.2 3D printing equipment modification and performance study of biphasic silicone ink

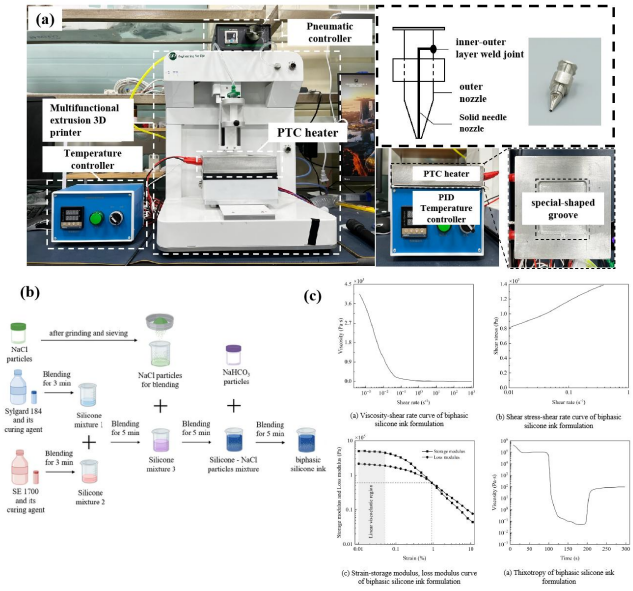


**Fig. 3 Bionic design and fabrication of the cartilage**

Unedited

**scaffold structure**

(a)3D printing equipment; (b) The preparation process of biphasic silicone ink; (c) The rheological properties of the biphasic silicone ink formulation

The printing equipment was equipped with a coaxial nozzle with a solid needle structure and an in-situ curing device (Fig. 3a) to enable molding of the hollow fiber. The apparatus employs two nozzles with different coaxialities and diameters, and is formed into a core shell structure through welding. Among these, the small diameter nozzle in the inner layer has a plugged hollow portion to form a solid needle-like structure. The outer nozzle model has an inner diameter of 0.85 mm, and an outer diameter of 1.25 mm; the inner nozzle model is 28G, has an inner diameter of 0.17 mm, and an outer diameter of 0.32 mm. The hollow fiber faces difficulties in forming when the biphasic silicone ink is printed at room temperature, and so intermediate collapse may occur in the hollow fiber, leading to low final molding quality. To avoid this, the in-situ curing device provides a high temperature environment for the biphasic silicone ink printing, which promotes rapid in-situ curing and supports the integrity of the structural molding. The in-situ curing device adopts a positive temperature coefficient (PTC) heater, which is composed of ceramic heating elements and aluminum tubing. Its working voltage is 220 V, its rated power is 600 W, and its overall dimensions are 170 mm × 140 mm × 30 mm. The pressure control unit of the built-in air pump is used to control the extrusion pressure.

The effects of various components in the biphasic silicone ink on its viscosity, shear stress, storage modulus, loss modulus, and thixotropy were investigated, and an optimized formulation of the ink for subsequent printing experiments was determined (Table 2). Additional methods and data regarding this investigation are provided in the **Supplementary Information.**

**Table 2 Composition and content of the biphasic silicone ink**

| Mass ratio of Sylgard 184 to SE 1700 | Average particle size of NaCl particles ( $\mu m$ ) | Total solid particle content (%) |
|---|---|---|
| 1：9 | 104.40 | 100 |

The preparation process of the biphasic silicone ink is illustrated in Fig. 3b. The relevant rheological properties of this custom-formulated ink were tested, with the results shown in Table 3 and Fig. 3c. Overall, the biphasic silicone ink has high viscosity, strong non-Newtonian effects, and a robust ability to maintain its own form, thus meeting the requirements of subsequent printing experiments.

**Table 3 Rheological properties of the biphasic silicone ink**

| Consistency coefficient [1)] | $n$[2)] | Yield stress (Pa) | $\tan\delta$ [3)] |
|---|---|---|---|
| 1,252.56 | 0.0304 | 819.33 | 0.4346 |

1）The consistency coefficient is used to evaluate the viscosity; the higher the value, the greater the viscosity.

2）n is the flow index, and the value of n is used to quantify the non-Newtonian behavior of the fluid. The larger the value of $||n|-1|$, the stronger the non-Newtonian behavior of the tested fluid, which is characterized by more pronounced shear thinning.

3）The loss factor is defined as the ratio of energy dissipated and stored per cycle, and is used to characterize the viscoelastic properties of the material, and is given by $\tan\delta = G'' / G'$, where G' and G'' are the energy storage modulus and energy dissipation modulus of the biphasic silicone ink, respectively.

### 3.3 Mechanical property control of the cartilage scaffold

Unedited

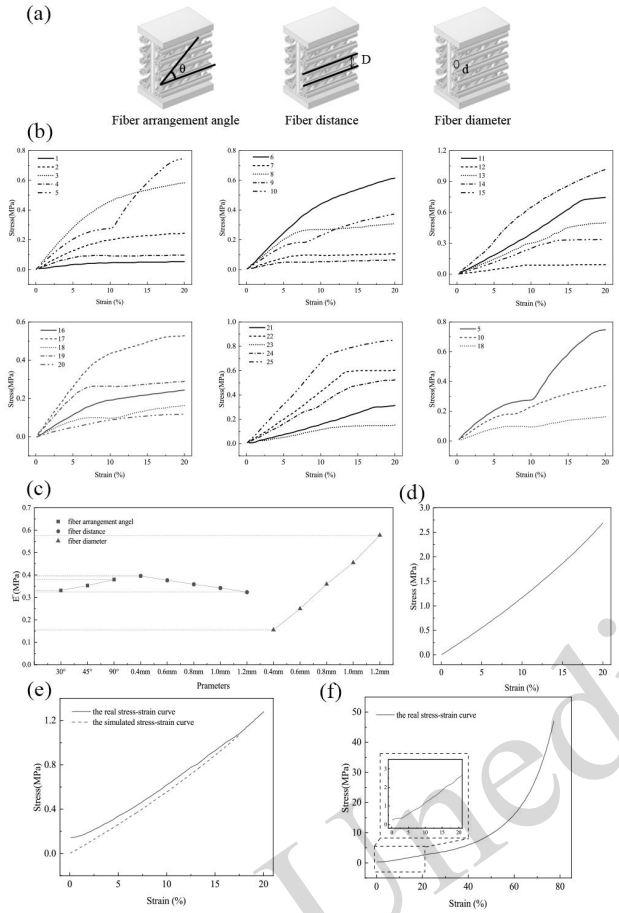


**Fig. 4 Mechanical properties of the cartilage scaffold**

(a) The three main structural parameters affecting the mechanical properties of the cartilage scaffolds; (b) Stress-strain curves of 25 groups of simulated cartilage scaffolds; (c) The simulated average compression modulus corresponding to each level of the three factors in the cartilage scaffold structural design; (d) The simulated stress-strain curve corresponding to the horizontal combination with the largest compression modulus; (e) A comparison between the real stress-strain curve and the simulated stress-strain curve; (f) The real stress-strain curve of the bionic four-region drug-loaded porous cartilage scaffold.

To analyze the mechanical compatibility between the cartilage scaffold and natural cartilage, the mechanical properties of the designed cartilage scaffold are studied in terms of three main structural parameters: fiber arrangement angle, fiber distance, and fiber diameter (Fig. 4a). To investigate the impact of each parameter on the mechanical properties of the cartilage scaffold, 25 simulation models were established using a mixed-level orthogonal experimental design, with one-factor three levels and two-factor five levels combined using the quasi-level method. Table 4 presents the scaffold model structural parameters and simulated compression modulus (E) results from the orthogonal experiment. Fig. 1a–e correspond to sequences 1-5 in Table 4; Fig. 1f–g correspond to sequences 6-10 in Table 4; Fig. 1k–o correspond to sequences 11-15 in Table 4; Fig. 1p–t correspond to sequences 16-20 in Table 4; and Fig. 1u–y correspond to sequences 21-25 in Table 4. During compression, the fiber layers parallel to the stress direction initially serve as the primary stress units until they are crushed, at which point the primary stress units become the fiber layers which are oriented at an angle to the stress direction.

Unedited

**Table 4 Structural parameters and simulated results on the cartilage scaffold structure**

| Number[1)] | Fiber arrangement angle (°) | Fiber distance (mm) | Fiber diameter (mm) | E (MPa) |
|---|---|---|---|---|
| 1 | 30 | 0.4 | 0.4 | 0.1585 |
| 2 | 30 | 0.6 | 0.8 | 0.3612 |
| 3 | 30 | 0.8 | 1.2 | 0.5633 |
| 4 | 30 | 1.0 | 0.6 | 0.1987 |
| 5 | 30 | 1.2 | 1.0 | 0.3741 |
| 6 | 45 | 0.4 | 1.2 | 0.6094 |
| 7 | 45 | 0.6 | 0.6 | 0.2542 |
| 8 | 45 | 0.8 | 1.0 | 0.4469 |
| 9 | 45 | 1.0 | 0.4 | 0.1377 |
| 10 | 45 | 1.2 | 0.8 | 0.3153 |
| 11 | 90 | 0.4 | 1.0 | 0.5310 |
| 12 | 90 | 0.6 | 0.4 | 0.1800 |
| 13 | 90 | 0.8 | 0.8 | 0.3665 |
| 14 | 90 | 1.0 | 1.2 | 0.5852 |

| | | | | |
|---|---|---|---|---|
| 15 | 90 | 1.2 | 0.6 | 0.2602 |
| 16 | 45 | 0.4 | 0.8 | 0.3874 |
| 17 | 45 | 0.6 | 1.2 | 0.5861 |
| 18 | 45 | 0.8 | 0.6 | 0.2413 |
| 19 | 45 | 1.0 | 1.0 | 0.4240 |
| 20 | 45 | 1.2 | 0.4 | 0.1249 |
| 21 | 90 | 0.4 | 0.6 | 0.2932 |
| 22 | 90 | 0.6 | 1.0 | 0.4998 |
| 23 | 90 | 0.8 | 0.4 | 0.1748 |
| 24 | 90 | 1.0 | 0.8 | 0.3646 |
| 25 | 90 | 1.2 | 1.2 | 0.5433 |
| $\overline{E}_{1-5}$ | 0.3311 | 0.3959 | 0.1552 | |
| $\overline{E}_{6-10}$ | 0.3527 | 0.3763 | 0.2495 | |
| $\overline{E}_{11-15}$ | 0.3846 | 0.3586 | 0.3590 | |
| $\overline{E}_{16-20}$ | 0.3527 | 0.3420 | 0.4551 | |
| $\overline{E}_{21-25}$ | 0.3751 | 0.3235 | 0.5774 | |
| R | 0.0534 | 0.0723 | 0.4223 | |

1) $\overline{E}_{1-5}$, $\overline{E}_{6-10}$, $\overline{E}_{11-15}$, $\overline{E}_{16-20}$, and $\overline{E}_{21-25}$ are the average values for compression moduli of 1-5, 6-10, 11-15, 16-20, and 21-25, respectively, and R represents ranges for fiber arrangement angle, fiber distance, and fiber diameter.

The orthogonal experiments yielded stress-strain curves for 25 simulated models (Fig. 4b). From these curves, it is evident that the stress-strain relationships for groups 5, 10, and 18 show gradually increasing trends – a phenomenon which is attributed to the specific angles of the fiber layers relative to the stress direction. The structural parameter-average compression modulus curve (Fig. 4c) indicates that the average compression modulus increases with fiber placement angle and fiber diameter, but decreases with fiber spacing. The influence of fiber diameter, fiber distance, and fiber arrangement angle on the average compression modulus were revealed as representing primary and secondary factors. The area of the shaded regions in Fig. 4a is used to determine the hierarchical relationship between the three structural parameters, which can also be assessed using the range values in Table 5. The larger the shaded area (or the greater the range values), the more dominant the structural parameter. Thus, the three structural parameters, ranked from primary to secondary, are fiber diameter, fiber distance, and fiber arrangement angle. When the fiber arrangement angle is 90°, the fiber distance is 0.4 mm, and the fiber diameter is 1.2 mm, the compression modulus is at a maximum. These structural parameters are then plugged into the model and the corresponding compression modulus is obtained. Fig. 4d shows the stress-strain curve of the simulation with the structural parameters corresponding to the maximum compression modulus. The compression modulus is 0.6553 MPa, which significantly exceeds the compression modulus of each group in Table 4.

Mechanical performance tests of the actual cartilage scaffold validated these simulation results. Within a small strain range of 0-20%, a comparison of the real and simulated stress-strain curves (Fig. 4e) reveals approximate linear behavior. The trend of the actual stress-strain curves aligns well with the simulations. The real compression modulus ($E_a$) was calculated as 0.6789 MPa. The discrepancy between the actual and simulated compression modulus is less than 5%, confirming the validity and accuracy of the established simulation.

**Table 5 Mechanical properties of articular cartilage**

| Compression modulus (MPa) | Young's modulus (MPa) | Poisson's ratio |
|---|---|---|
| 0.24-0.85 | 5-25 | 0.06-0.3 |

To ensure that the designed cartilage scaffold exhibits structural and functional compatibility with native cartilage tissue, ideal structural parameters for the scaffold were determined through simulation of the mechanical parameters and functions of various regions of native cartilage. It was determined that the

Unedited

superficial region should have the smallest fiber diameter, with vertically crossed fibers. The transitional region should possess relatively large fiber diameters and a substantial number of diagonal fibers so as to resist compressive stresses, with its compression modulus being second only to that of the radial region. The radial region should feature vertically aligned coarse fibers, as this is the primary structure for resisting compressive stress and must have the highest compression modulus. The calcified cartilage layer should form a relatively dense structure. Table 6 details the structural parameters for each region of the four-region drug-loaded integrated porous cartilage scaffold.

The true stress-strain curves of the cartilage scaffold samples, printed according to the structural parameters in Table 4 (Fig. 4f), demonstrate that within a large strain range of 0-80%, stress is positively and nonlinearly correlated with strain. Within a small strain range of 0-20%, the stress-strain curves are approximately linear. The actual compression modulus ($E_b$) was calculated as 0.8291 MPa, falling within the range of joint cartilage as shown in Table 5. The results show that the bionic four-region cartilage scaffold matches well with native cartilage in terms of mechanical properties, and might therefore effectively replace cartilage in this regard.

**Table 6 The structural parameters of the four-region biomimetic drug-laden cartilage scaffold ink**

| Region | Region Proportion (%) | Fiber Diameter (mm) | Fiber Distance (mm) | Fiber Arrangement angle (°) |
|---|---|---|---|---|
| The superficial region | 10 | 0.8 | 0.4 | 90 |
| The transitional region | 40 | 1.0 | 0.4 | 45 |
| The radial region | 30 | 1.2 | 0.4 | 90 |
| The region of calcified cartilage | 20 | 1.2 | 0.2 | 0 |

### 3.4 Characterization of drug loading, sustained drug release performance, and biocompatibility of the cartilage scaffold

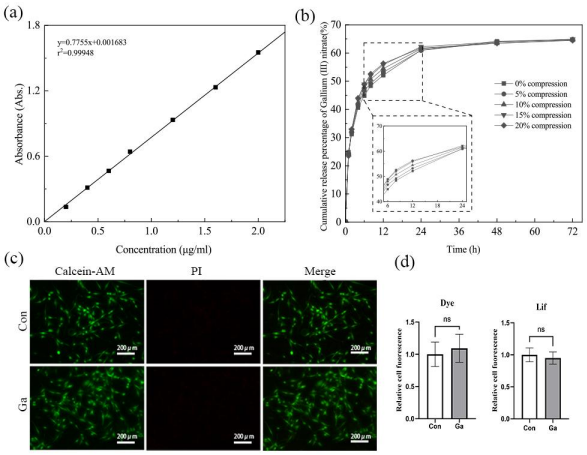


**Fig. 5 Characterization of drug loading, sustained drug release performance, and biocompatibility of the cartilage scaffold**

(a)The standard curve of gallium nitrate (III) complex at the maximum absorption peak; (b) Time curve of cumulative percentage release of gallium nitrate (III); (c) Live/dead staining fluorescence microscope images of human chondrosarcoma cells cultured on a cartilage scaffold for 48 hours (scale bar = 200 μm).

In order to characterize the drug release performance of the cartilage scaffold, a compression experiment on the scaffold was designed to simulate the environment of in-vivo implantation. The drug release performance was characterized by measuring the content of gallium nitrate in the solution following the compression test, and calculating the cumulative release percentage of gallium nitrate for each measurement. A UV spectrophotometer was used to determine the concentration of gallium nitrate, because gallium nitrate solution reacts with rhodamine B under acidic conditions, there is a maximum absorption peak in the UV spectrum when scanned by the spectrophotometer, and the standard curve measured under this maximum absorption peak has a clear linear relationship. Therefore, the concentration of gallium nitrate can be evaluated according to the concentration of the gallium nitrate (III) complex, in order to characterize the drug-loading and slow-release performance of the scaffold. The maximum absorption peak of the complex was 556 nm, as measured by full spectrum scanning with the UV spectrophotometer. According to the standard curve of gallium nitrate (III) complex (Fig. 5a), the regression equation for gallium nitrate (III) complex is y = 0.7755x + 0.001683, and the

Unedited

correlation coefficient R2 is 0.99948. These results reveal that the concentration of gallium nitrate (III) complex has a clear linear relationship with absorbance in the range of 0.2 ~ 2 μg/mL.

We next conducted compression experiments at various rates to evaluate the drug release performance of the scaffold under different compression conditions. The experimental results demonstrated that gallium nitrate (III) in the scaffold was gradually released at a high rate to a level of about 50% within 0-8 hours, and then the release rate gradually decreased until 72 hours, where the maximum cumulative release rate remained at approximately 65%. This indicates that the scaffold's drug release functionality is relatively stable, enabling rapid release to a desired concentration and maintenance of this concentration for a certain period. As the amount of compression increases, the rate of drug release gradually increases, and the time required to reach the maximum cumulative release percentage decreases. Moreover, no matter how the compression amount changes, the maximum cumulative release percentage remains stable. This phenomenon reflects the stability of the scaffold's drug release functionality, since slight deformation does not significantly alter the drug release effects.

To determine whether gallium nitrate-bearing scaffolds negatively impact normal cartilage cells during drug release, we performed cytotoxicity tests on the surface of porous materials containing gallium ions, and on control materials of the same shape (without gallium ions). As shown in Fig. 5c, after 48 hours of culturing of human chondrosarcoma cells on cartilage scaffold samples, living cells showed green fluorescence under Calcein-AM staining, while dead cells showed red fluorescence under PI staining. Cell survival on the cartilage scaffold sample surfaces was high, regardless of the presence or absence of gallium nitrate, indicating that scaffolds containing gallium nitrate have similarly small cytotoxicity compared to scaffolds without gallium nitrate.

## 5 Conclusions

In this study a novel biomimetic four-region drug-laden porous cartilage scaffold was developed for the treatment of cartilage defects. To achieve structural and functional compatibility with native cartilage, the scaffold was designed with a biomimetic hollow porous fiber network with optimized structural parameters. The ideal structural parameters were determined through parameter-stress simulations. The scaffold's morphology was examined using scanning electron microscopy (SEM), revealing a porosity of 60.19%. Additionally, the compression modulus of the designed cartilage scaffold (E = 0.8291 MPa) was found to closely match that of native cartilage tissue. In-vitro drug release performance was assessed using UV spectrophotometry, and revealed a trend of initial rapid release followed by sustained concentration; moreover, minor scaffold deformations were found to not significantly impact the drug release effects. Finally, the scaffold's biocompatibility was evaluated by placing human chondrosarcoma cells (SW 1353) on the scaffold surface and conducting live/dead assays. The findings indicated that the scaffold had no negative effects on the human chondrosarcoma cells. Through comprehensive analysis of varying performance characteristics, the feasibility and effectiveness of the proposed biomimetic four-region drug-laden porous cartilage scaffold was demonstrated.

Although the experimental results showcase the considerable potential of the scaffold for cartilage treatment, several key challenges must be addressed prior to clinical application. Improved scaling of production is critical for clinical application, since the scaffolds would need to be produced in sufficient quantity and with consistent quality. Also, it should be noted that the biomimetic design of the studied cartilage scaffolds primarily focused on mechanical properties and drug delivery. To better mimic native cartilage, additional complex functions such as wear resistance, buffering, and lubrication need to be incorporated. Therefore, scaffolds that achieve effective mechanical performance and biological functionality must also undergo rigorous in-vivo evaluations to assess their long-term biocompatibility, stability, and efficacy.

**Acknowledgments**

This work was financially supported by the National Natural Science Foundation of China (no. 52175278).

Unedited

## Declaration of interests

The authors declare no competing interests.

## Data availability

The data that support the findings of this study are available from the corresponding author upon reasonable request.

## References


Cai J, Chen Y, Liu Y, et al., 2022. Capillary imbibition and flow of wetting liquid in irregular capillaries: A 100-year review. *ADVANCES IN COLLOID AND INTERFACE SCIENCE*, 304 https://doi.org/10.1016/j.cis.2022.102654

Chen P, Tao J, Zhu S, et al., 2015. Radially oriented collagen scaffold with sdf-1 promotes osteochondral , by facilitating cell homing. *BIOMATERIALS*, 39:114-123. https://doi.org/10.1016/j.biomaterials.2014.10.049

Da H, Jia S-J, Meng G-L, et al., 2013. The impact of compact layer in biphasic scaffold on osteochondral tissue engineering. *PLOS ONE*, 8(1):e54838. https://doi.org/10.1371/journal.pone.0054838

Du Y, Liu H, Yang Q, et al., 2017. Selective laser sintering scaffold with hierarchical architecture and gradient composition for osteochondral repair in rabbits. *BIOMATERIALS*, 137:37-48. https://doi.org/10.1016/j.biomaterials.2017.05.021

Getgood AMJ, Kew SJ, Brooks R, et al., 2012. Evaluation of early-stage osteochondral defect repair using a biphasic scaffold based on a collagen-glycosaminoglycan biopolymer in a caprine model. *KNEE*, 19(4):422-430. https://doi.org/10.1016/j.knee.2011.03.011

Gu Z, Wang J, Fu Y, et al., 2023. Smart biomaterials for articular cartilage repair and regeneration. *Advanced Functional Materials*, 33(10):2212561. https://doi.org/https://doi.org/10.1002/adfm.202212561

Han G, Lee H, Kang JM, et al., 2023. 3d-printed nir-responsive bullets as multifunctional nanodrug platforms for image-guided local chemo-photothermal therapy. *Chemical Engineering Journal*, 477:147083. https://doi.org/https://doi.org/10.1016/j.cej.2023.147083

Hua Y, Huo Y, Bai B, et al., 2022. Fabrication of biphasic cartilage-bone integrated scaffolds based on tissue-specific photo-crosslinkable acellular matrix hydrogels. *MATERIALS TODAY BIO*, 17 https://doi.org/10.1016/j.mtbio.2022.100489

J.X. Liu GLG, G.R. Zhang, S.C. Min, H.T. Dong, L.P. An, 2019. Long-term follow-up of autologous osteochondral transplantation for knee cartilage defects. *China Orthop Trauma*, 32(4):346-349.

Kim S-Y, Han G, Hwang D-B, et al., 2021. Design and usability evaluations of a 3d-printed implantable drug delivery device for acute liver failure in preclinical settings. *Advanced Healthcare Materials*, 10(14):2100497. https://doi.org/https://doi.org/10.1002/adhm.202100497

Kwon H, Brown WE, Lee CA, et al., 2019. Surgical and tissue engineering strategies for articular cartilage and meniscus repair. *NATURE REVIEWS RHEUMATOLOGY*, 15(9):550-570. https://doi.org/10.1038/s41584-019-0255-1

Levingstone TJ, Ramesh A, Brady RT, et al., 2016a. Cell-free multi-layered collagen-based scaffolds demonstrate layer specific regeneration of functional osteochondral tissue in caprine joints. *BIOMATERIALS*, 87:69-81. https://doi.org/10.1016/j.biomaterials.2016.02.006

Levingstone TJ, Thompson E, Matsiko A, et al., 2016b. Multi-layered collagen-based scaffolds for osteochondral defect repair in rabbits. *Acta Biomaterialia*, 32:149-160. https://doi.org/10.1016/j.actbio.2015.12.034

Li X, Zhao Y, Zhao C, 2021. Applications of capillary action in drug delivery. *ISCIENCE*, 24(7) https://doi.org/10.1016/j.isci.2021.102810

Liu H, Cheng Y, Chen J, et al., 2018. Component effect of stem cell-loaded thermosensitive polypeptide hydrogels on cartilage repair. *Acta Biomaterialia*, 73:103-111. https://doi.org/https://doi.org/10.1016/j.actbio.2018.04.035

Liu J, Li L, Suo H, et al., 2019. 3d printing of biomimetic multi-layered gelma/nha scaffold for osteochondral defect repair. *MATERIALS & DESIGN*, 171 https://doi.org/10.1016/j.matdes.2019.107708

Malda J, Groll J, Van Weeren PR, 2019. Rethinking articular cartilage regeneration based on a 250-year-old statement. *NATURE REVIEWS RHEUMATOLOGY*, 15(10):571-572. https://doi.org/10.1038/s41584-019-0278-7

Parisi C, Salvatore L, Veschini L, et al., 2020. Biomimetic gradient scaffold of collagen-hydroxyapatite for osteochondral regeneration. *JOURNAL OF TISSUE ENGINEERING*, 11 https://doi.org/10.1177/2041731419896068

Pattnaik A, Sanket AS, Pradhan S, et al., 2023. Designing of gradient scaffolds and their applications in tissue regeneration. *BIOMATERIALS*, 296 https://doi.org/10.1016/j.biomaterials.2023.122078

Schizas N, Savvidou O, Triantafyllopoulos I, et al., 2019. Adjuvant therapies for the enhancement of microfracture technique in cartilage repair. *ORTHOPEDIC REVIEWS*, 11(3):148-153. https://doi.org/10.4081/or.2019.7950

Shen C, Wang J, Li G, et al., 2024. Boosting cartilage repair with silk fibroin-DNA hydrogel-based cartilage organoid precursor. *Bioactive Materials*, 35:429-444. https://doi.org/https://doi.org/10.1016/j.bioactmat.2024.02.016

Soleymani M, Motiee E-S, Karbasi S, et al., 2024. Evaluation of the effects of decellularized umbilical cord wharton's jelly ecm on polyhydroxy butyrate electrospun scaffolds: A new strategy for cartilage tissue engineering. *MATERIALS TODAY CHEMISTRY*, 39 https://doi.org/10.1016/j.mtchem.2024.102145

Sun Z, Bonassar LJ, Putnam D, 2020. Influence of block length on articular cartilage lubrication with a diblock bottle-brush copolymer. *ACS APPLIED MATERIALS & INTERFACES*, 12(1):330-337.


Unedited

https://doi.org/10.1021/acsami.9b18933
Wang M, Wu Y, Li G, et al., 2024a. Articular cartilage repair biomaterials: Strategies and applications. *MATERIALS TODAY BIO*, 24:100948. https://doi.org/https://doi.org/10.1016/j.mtbio.2024.100948
Wang W, Li H, Song P, et al., 2024b. Photo-crosslinked integrated triphasic scaffolds with gradient composition and strength for osteochondral regeneration. *JOURNAL OF MATERIALS CHEMISTRY B*, 12(5):1271-1284. https://doi.org/10.1039/d3tb02031b
Yang H, Zheng M, Zhang Y, et al., 2024a. Enhanced angiogenesis in porous poly(ε-caprolactone) scaffolds fortified with methacrylated hyaluronic acid hydrogel after subcutaneous transplantation. *BMT*, 5(1) https://doi.org/10.12336/biomatertransl.2024.01.006
Yang S, Wu H, Peng C, et al., 2024b. From the microspheres to scaffolds: Advances in polymer microsphere scaffolds for bone regeneration applications. *BMT*, 5(3) https://doi.org/10.12336/biomatertransl.2024.03.005
Zhang X, Yan Z, Guan G, et al., 2022. Polyethylene glycol diacrylate scaffold filled with cell-laden methacrylamide gelatin/alginate hydrogels used for cartilage repair. *JOURNAL OF BIOMATERIALS APPLICATIONS*, 36(6):1019-1032. https://doi.org/10.1177/08853282211044853
Zhang Y, Liu X, Zeng L, et al., 2019. Polymer fiber scaffolds for bone and cartilage tissue engineering. *Advanced Functional Materials*, 29(36):1903279. https://doi.org/https://doi.org/10.1002/adfm.201903279
Zhou B XP, Li X,Gong Y, Shen D, 2005. Spectrophotometric determination of gallium nitrate content in gallium nitrate injection. *Journal of Chinese Pharmaceutical Sciences*, (01):30-31.

## 中文概要

**题　目：仿生四区域药物负载软骨支架的设计与制造**

**作　者：**陈语[1,2]，马宇哲[1,2]，傅建中[1,2]，姚鑫骅[1,2]

**机　构：**[1]浙江大学，流体动力与机电系统国家重点实验室，中国杭州，310058；[2]浙江大学，浙江省3D打印工艺与装备重点实验室，中国杭州，310058

**目　的：**关节软骨是关节功能的关键组成部分，但由于外伤和退行性疾病的影响，软骨极易受到损伤。传统的软骨治疗方法通常依赖复杂的手术程序，且疗效有限。作为一种潜在的替代方案，植入式载药支架逐渐成为一种有前景的软骨疾病治疗选择。然而，支架与天然软骨在结构与功能上的兼容性问题以及载药缓释功能的优化，仍然是当前面临的重大挑战。为了解决这些问题，本文提出了一种采用四区域中空多孔纤维网络结构的新型软骨支架设计。该支架使用液相硅胶和固体颗粒组成的双相硅胶墨水，利用挤出式3D打印平台制备。支架的单轴压缩实验结果表明，该软骨支架在力学性能上与天然软骨相似；紫外分光光度测试则验证了其具备可控的药物释放能力。研究表明，所提出的软骨替代结构在可行性和效果方面均展现出良好的潜力。

**创新点：**1. 提出了一种具有良好自支撑性能的双相有机硅油墨配方；2. 提出了一种软骨支架的仿生设计，使支架具有与天然软骨相似的力学性能；3.软骨支架集成了由中空多孔纤维组成的药物输送系统，保证了稳定的药物释放性能。

**方　法：**1. 通过建模仿真，建立软骨支架压缩力学性能的数值模型（图4）；2. 通过正交实验，确定软骨支架的纤维直径、纤维间距、纤维排列角等结构设计参数（表4）。

**结　论：**1. 设计的仿生四区域中空多孔药物载体支架在结构与功能上高度接近天然软骨，具备良好应用前景；2. 设计的支架具备初始快速释放及后期持续释放的药物释放特性；3. 通过生物相容性实验表明，支架具有良好的生物相容性。

**关键词：**仿生设计；3D打印；软骨支架；梯度多孔结构；力学性能调控；药物释放系统

Uncedited